Tenth International Conference on Computational Fluid Dynamics (ICCFD10), Barcelona, Spain, July 9-13, 2018 **ICCFD10-071**

ANSYS CFD Validation for Civil Transport Aircraft in High-Lift Configuration Part-1

Krishna Zore[1]
ANSYS Software Pvt Ltd, Plot no. 34/1, Hinjewadi, Pune - 411057, Maharashtra, India

Shoaib Shah[2], John Stokes[3]
ANSYS Canada Ltd., 1000 Sherbrooke Street West, Suite 2120, Montreal QC, H3A 3G4 Canada

Balasubramanyam Sasanapuri[4]
ANSYS Software Pvt Ltd, Unit no. 906, The Platina, Gachibowli, Hyderabad 500032, India

Patrick Sharkey[5]
ANSYS UK Ltd., 97 Jubilee Avenue, Milton Park Oxfordshire OX14 4RW United Kingdom

Abstract: The paper presents a study of aerodynamic flow computations over a civil transport aircraft high-lift configuration model performed using ANSYS Fluent – a cell-centered, Reynolds-averaged Navier-Stokes CFD solver. The computational results obtained on the JAXA Standard Model (JSM)[1] are validated against experimental data from JAXA's Low Speed Wind Tunnel (JAXA-LWT1). In Part 1, the model is studied in a nominal landing configuration with high-lift devices deployed including the support brackets. The study including an under-wing mounted engine-nacelle-pylon on the JSM will be presented in a second paper as Part-2. The JSM CAD geometry cleanup and part-management is performed using ANSYS SpaceClaim Direct Modeler (SCDM) R18.2, and the unstructured hybrid mesh is generated using ANSYS Fluent Meshing R18.2. Comparison between ANSYS Fluent R18.2 computational results and experimental data over a sweep of angles of attack will be shown based on aerodynamic forces, moments and pressure coefficients as well as surface flow visualizations. The fully turbulent results based on the Shear Stress Transport k-ω (SST)[5,6] turbulence model and the transition results using SST-Transition (γ-Re_θ)[7] model will be discussed.

Keywords: High-Lift Aerodynamics, Computational Fluid Dynamics (CFD), Computer-Aided Design (CAD), Turbulence Modeling, Transition, American Institute of Aeronautics and Astronautics, Japan Aerospace Exploration Agency (JAXA).

1 Introduction

Development of efficient high-lift devices for take-off and landing are a very important part of the aircraft design process and have a strong influence on aircraft performance and operational costs. For a large commercial transport aircraft with twin jet engines, an improvement of 1% in lift-to-drag ratio at takeoff can provide a 1270 kg (2800-lb) increase in payload, whereas, an improvement of 1.5% in maximum lift coefficient at landing can provide a 3000 kg (6600-lb) increase in payload[1]. Today's CFD codes are highly reliable and consistent for simplified cruise-type configurations,

---

[1] Application Software Development
2 Senior Software Development
3 Director Software Development
4 Lead Technology Specialist, Senior AIAA Member
5 Lead Software Development

however, the complexities associated with the high-lift configurations make it very challenging to predict high-lift aerodynamic forces accurately[2,12,13,15]. One of the main challenges in CFD modelling of high-lift systems is mesh generation, due to the complex multi-element wing system comprising slat, main-wing and flap elements (in addition to support brackets and numerous small gaps). Another challenge is the complexity of flow physics itself, with numerous phenomena such as boundary-layer transition, flow separation, reattachment and wake-boundary layer interaction all playing an important role[2,3,10,11]. Careful resolution of such phenomena and together with the CFD flow solver accuracy are critical to the accurate prediction of aerodynamic forces required for the development of an efficient aerodynamic design system.

ANSYS Fluent solver's high-lift aerodynamic prediction capabilities are validated on the JAXA Standard Model (JSM) in its nominal landing configuration, with high-lift devices including support structures such as the slat tracks and Flap Track Fairings (FTF) deployed. This model was tested at the *6.5m x 5.5m* JAXA- Low Speed Wind Tunnel (LWT1)[9]. The geometry, flow operating conditions and experimental data are taken from NASA's 3rd AIAA CFD High Lift Prediction Workshop[4]. Geometric cleanup, part management and creation of volume mesh refinement regions known as body of influences (BOIs), are created in ANSYS Spaceclaim Direct Modeler (SCDM) R18.2. Unstructured surface (triangular facets) and hybrid volume (prisms and tetrahedrons) meshes are generated using ANSYS Fluent Meshing R18.2. Finally, computational results obtained with ANSYS Fluent R18.2 using turbulence models both with and without laminar-turbulent transition are validated against experimental data.

2 Model Geometry Preparation

The JSM in nominal landing configuration (slat and flap deployed at 30^0) with support brackets (such as the slat tracks and FTFs) is shown in Figure 1. The geometric reference parameters for the JSM are outlined in Table 1.

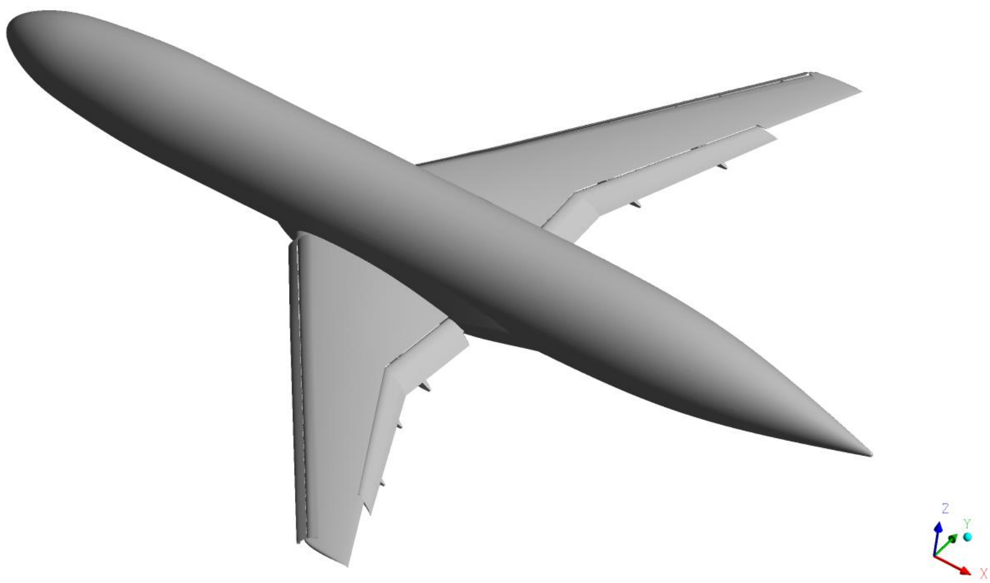

Figure 1: JSM, wing-body configuration

Table 1. JSM Geometry parameters.

Geometric parameters	Units
Mean aerodynamic chord (MAC)	529.2 mm **model scale**
Wing semi-span	2300.0 mm
Reference area of the semi-span model ($S_{ref}/2$)	1123300.0 mm2
Moment reference center (MRC)	x = 2375.7 mm, y = 0.0 mm, z = 0.0 mm

The ‘watertight’ geometry required for CFD mesh generation is created using the multi-purpose ANSYS 3D SCDM. A built-in repair toolkit with simple and easy-to-use utilities, such as stitching, and gap and missing faces detection, quickly addresses any minor CAD incongruities and improve CAD fidelity. The “Design Sketch” tool is used to create Bodies of Influence (BOIs) for subsequent use during mesh generation, to obtain better volume mesh refinement control. These BOIs are especially important where the propensity of complex flow behavior is expected around the slat tracks, FTFs, multi-element wing gaps, wing-body junction, wing-slat-flap tips and in the high-lift system wakes. Figure 2 shows these refinement regions. The box-shaped farfield domain enclosing the JSM is created using the “Prepare-Enclosure” utility tool. To avoid farfield boundary effects on the JSM, the farfield extends to 100 times the MAC length. Additionally, surface grouping is done using “Groups” utility, so that during mesh generation, local surface mesh size controls can be directly applied in areas such as the leading and trailing edges of multi-element wing, high curvature areas, wing-slat-flap tips, wing-body junction, slat tracks, FTFs, fuselage nose and rear. Once the geometry is prepared, it is saved in *SCDOC* format (SCDM native file format) and imported into ANSYS Fluent Meshing.

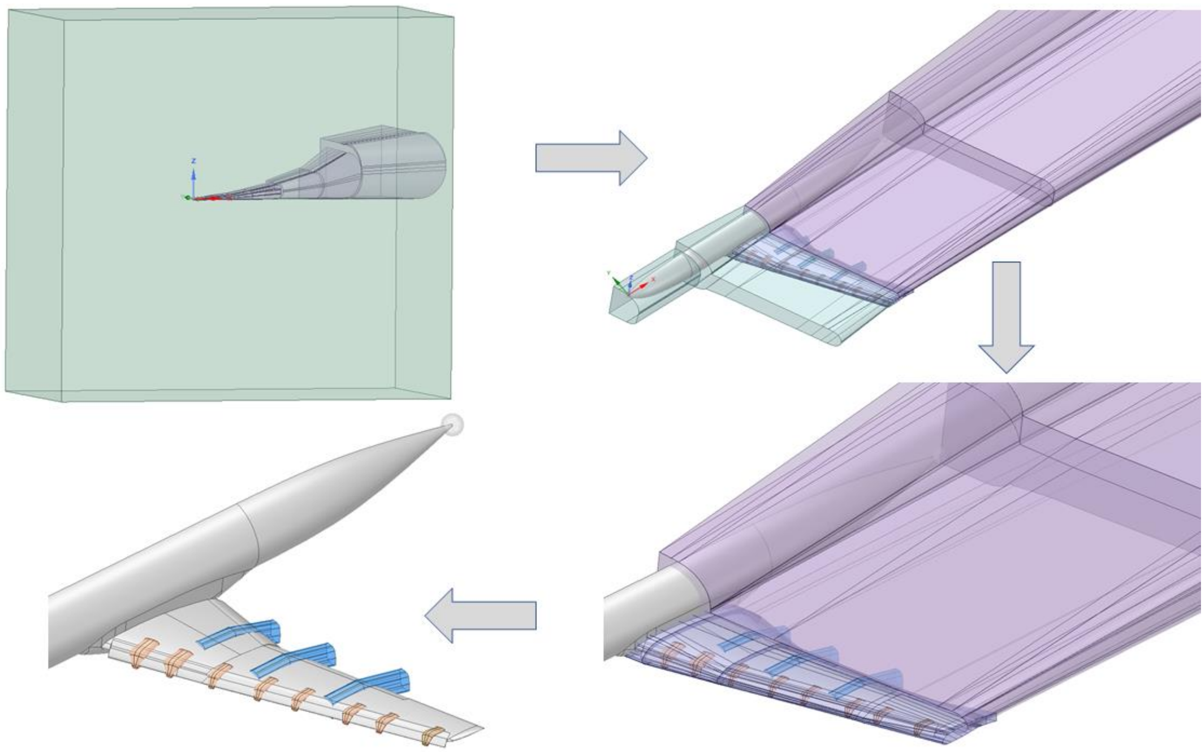

Figure 2: JSM, farfield domain, and BOI (refinement) regions.

3 Mesh Generation

ANSYS Fluent Meshing is a robust, unstructured hybrid mesh generation tool which can create meshes of virtually any size or complexity, consisting of tetrahedral, hexahedral, polyhedral, prismatic, or pyramidal cells.

ANSYS Fluent Meshing can generate unstructured tetrahedral, hex-core, or hybrid volume CFD meshes, primarily using two approaches: using an existing surface mesh topology from any other mesh generation tool or using a combination of the “CAD Faceting” and “CFD Surface Mesh” options to create an initial, ‘watertight’ surface grid. Either approach serves as the basis from which a high-quality volume mesh can be generated quickly and efficiently.

In this case, the second approach is followed: the JSM geometry is first imported into ANSYS Fluent Meshing using the “CAD Faceting” option as a “Mesh Object” feature, which results in a rough, faceted surface representation of the model. While this model is not suitable for volume mesh generation, it allows for a quick setup of meshing parameters. Local “Scoped Size Functions” are then defined on the imported model surfaces to provide better control on surface mesh distribution. Multiple surface mesh size control functions are available such as ‘*soft*’, ‘*hard*’, ‘*curvature*’ and ‘*proximity*’ based, all together controlling the maximum and minimum surface mesh size, surface curvature, and the number of cells per gap or between proximity edges/surfaces. Further adjustments in sizing can be made by computing a “size field” which provides a visual cue for the surface mesh sizes. On obtaining the desired surface mesh sizes, the “size field” file is saved and will be used to generate the triangulated surface mesh. This is done by re-importing the JSM CAD with the “CFD Surface Mesh” option and the “size field” file specified. On completion, the triangular surface mesh will appear under “Mesh Objects” ready for the volume mesh generation step.

For this study, a hybrid volume mesh consisting of prism layers above the wall boundaries (to capture the boundary layer) and isotropic tetrahedral cells filling the remaining volume is created. The prism layers are generated using a “Uniform” growth option by maintaining a constant initial height of 0.002 mm and a specified prism growth ratio ranging from 1.1 (wing) to 1.2 (body). To avoid very thin prism elements, the aspect ratio is restricted using a prism control parameter. Additionally, a “Gap Factor” value is adjusted to maintain enough space for tetrahedral elements in proximity regions. To save time, prism-layer generation is done on parallel processors using automatic partitioning. The previously-generated “size field” file can be applied to the tetrahedral volume mesh sizing. Additional BOI sizing is required for extra refinement in key complex flow regions identified earlier. The final overall quality of the volume mesh is then improved using the “Auto Node Move” smoothing operation. The unstructured hybrid surface and volume mesh resolution are shown in Figure 3 while the mesh metrics for the JSM are shown in Table 2.

Table 2. JSM mesh metrics.

JSM configuration	Number of nodes	Number of cells	Initial wall spacing, Δy (normal dist.)	Number of cells on trailing edges
wing-body	125,670,996	289,270,572	0.002 mm	12

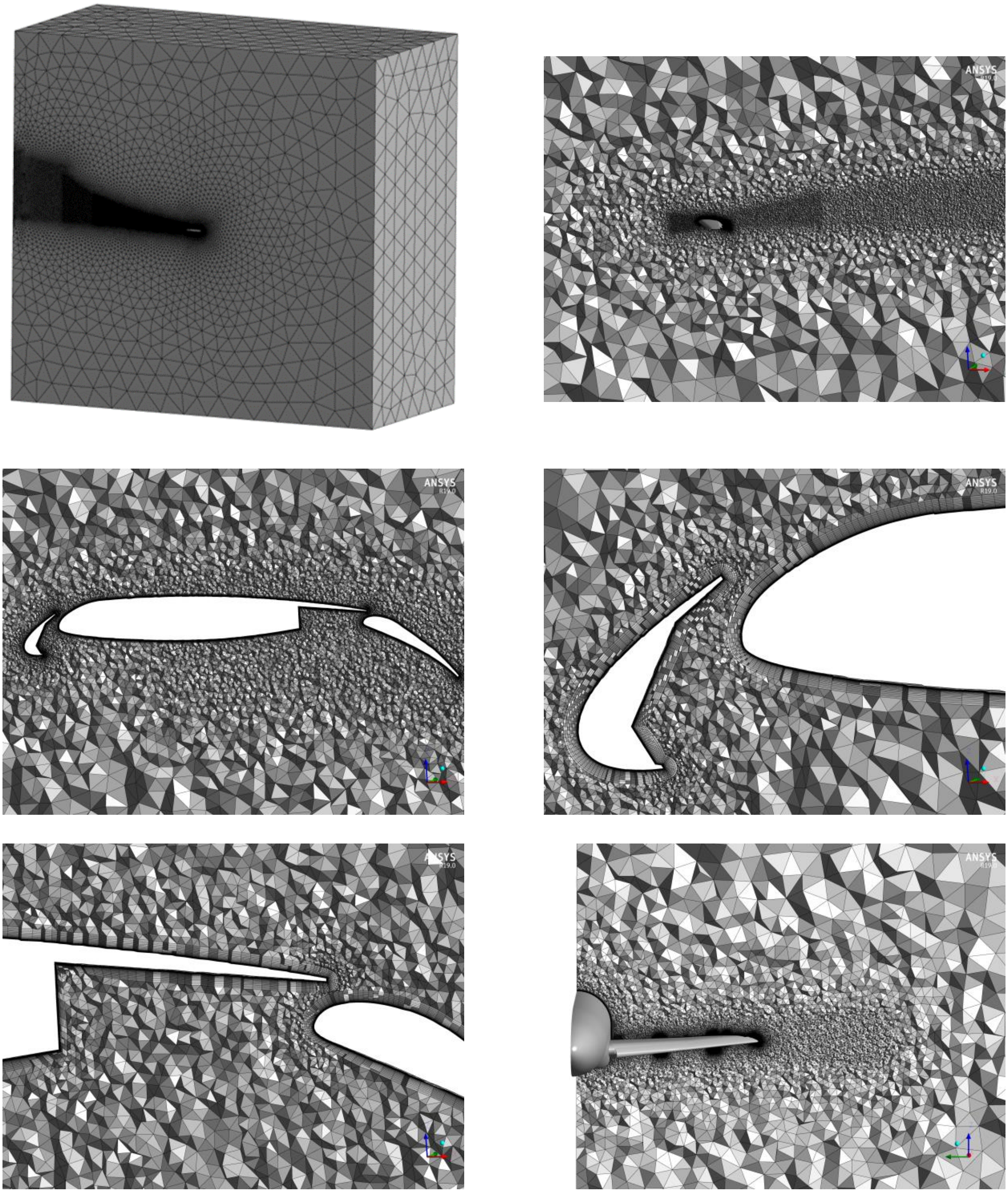
ANSYS

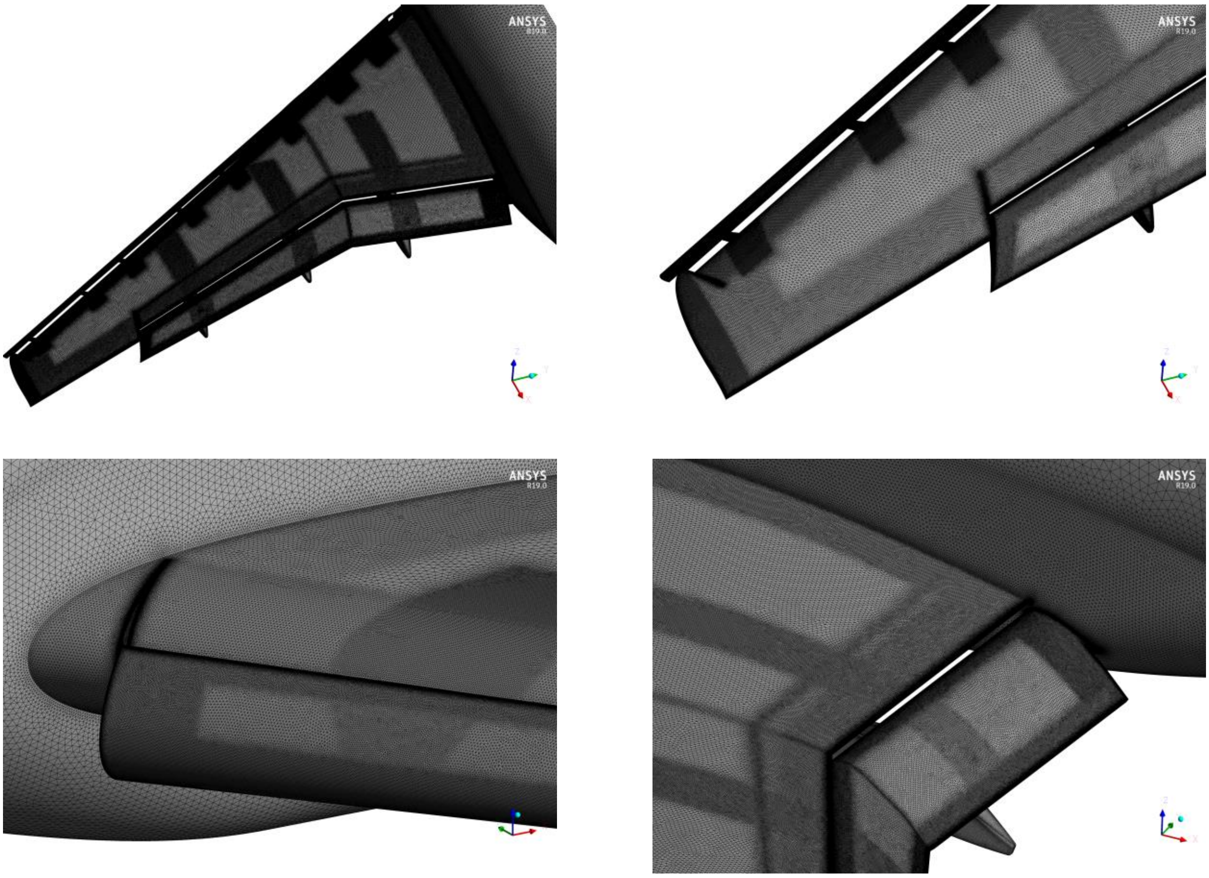

Figure 3: JSM, Computational mesh - cross-sectional and surface resolutions.

4 Flow Conditions and Solver

The wind tunnel flow conditions are outlined in Table 3 including the flow Mach number and angles of attack (α) sweep. For CFD, all simulations are "free air", and no wind tunnel walls or model support systems are included.

Steady-state RANS simulations were performed with ANSYS Fluent R18.2, a cell-centered finite volume method solver. A pressure-based fully coupled algorithm is employed with second order upwind and central discretization methods used for convective and diffusion terms, respectively. The resulting discrete linear system is solved using a point implicit (Gauss-Seidel) linear equation solver in conjunction with an algebraic multigrid (AMG) method. Turbulence was modelled using the k-ω Shear Stress Transport (SST)[5,6] model, while transition was modeled using the two-equation SST-Transition model (γ-Re_θ)[7]. Additionally, the models' constant *a1* was modified from 0.31 (*default*) to 1, as early tests on this case with the current meshes using *a1=1* resulted in separation being delayed to be more consistent with available experimental observations. It should be noted, however, that using the *default* SST model required further investigation (not done for this paper) looking at the effect of mesh resolution[21].

Table 3. JSM flow parameters.

Mach Number	0.172
Angles of attack (α)	4.36°, 10.47°, 14.54°, 18.58°, 20.59°, and 21.570°
Reynolds Number based on MAC	1.93 million
Reference Static Temperature	551.79°R (33.40°C or 92.12°F)
Reference Static Pressure	747.70 mmHg (14.458 PSI)

5 Results and Discussions

The JSM is solved at six angles of attack (α). The complete ANSYS Fluent solution analysis matrix for this study is shown in Table 4.

Table 4. JSM solution matrix.

JSM configuration	Turbulence models	Angles of attacks
Wing-body	SST *a1=1*	4.36°, 10.47°, 14.54°, 18.58°, 20.59°, 21.57°
	Transition-SST *a1=1*	

The computational results obtained on the JSM are validated against experimental data from JAXA's LWT1[4,9,10].

5.1 Aerodynamic Coefficient Comparisons

Figure 4 shows the C_L-α, C_D-α, C_L-C_D and C_L-C_M plot comparisons for JSM wing-body with experimental data. Both the computational results with SST *a1=1* and SST-Transition *a1=1* show good agreement with the experimental data at α = 18.58^0 and below.

Both SST *a1=1* and SST-Transition *a1=1* models predict stall occurring at α = 18.58^0 with C_{Lmax} = 2.746 and C_{Lmax} = 2.811, respectively, while the experiment shows stall at α = 20.59^0 and C_{Lmax} = 2.768. In general, for angles below 18.58^0, both models predict C_L within ~0.1 – 1.0% of the experiment. The Transition-SST *a1=1* model provides an overall better agreement of C_L at the non-linear portion of the C_L-α plot, but the overall C_L comparisons are generally very close.

The differences in drag between the two models are also generally very close. However, both C_D-α, and C_L-C_D plots indicate much more pronounced differences between wind tunnel and computational results, especially at α = 10.47^0 and higher. In general, the Transition-SST *a1=1* model provides slightly higher drag values compared to SST *a1=1*. Prior to stall, total drag differs from the experiments by ~10-60 drag counts with both models.

The C_L-C_M plots show that the nose down pitching moments are lower for the SST *al=1* model than for the Transition-SST *a1=1* model, with the latter generally producing better comparisons to experiment.

These observed differences are possibly due to insufficient grid resolution in areas of highly complex flow structures found in high-lift configurations. These areas include trailing edge wakes, support bracket wakes, wing-body junction flow, slat and flap cove vortices, wing tip vortices and other secondary spiral vortices. Some of the key areas where further refinement is needed will be discussed at the end of this section. Another possible reason for the differences could be the inherent limitation of linear eddy-viscosity turbulence models, which neglect the non-linear effects of turbulent, secondary and swirling flows. There is also an important possible impact of setting *a1=1* on the eddy viscosity term: while it prevents the onset of early flow separation (as compared to SST with *default a1*), it appears to lead to the higher drag predictions[21]. These possibilities all point to the need for further investigation to fully understand the mesh requirements, turbulence modeling needs, and complex flow behavior associated with such multi-element high-lift devices, especially in the presence of supporting brackets.

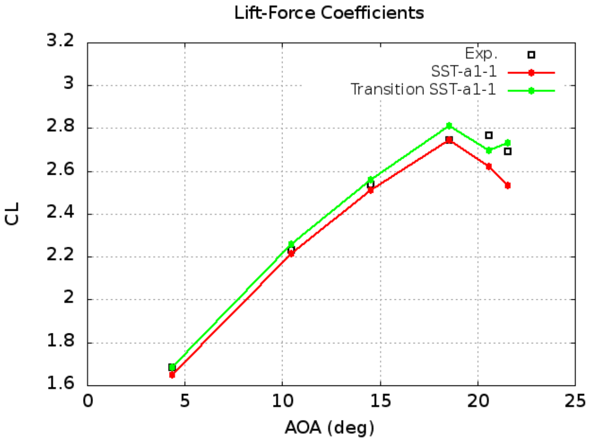

(a) C_L vs α.

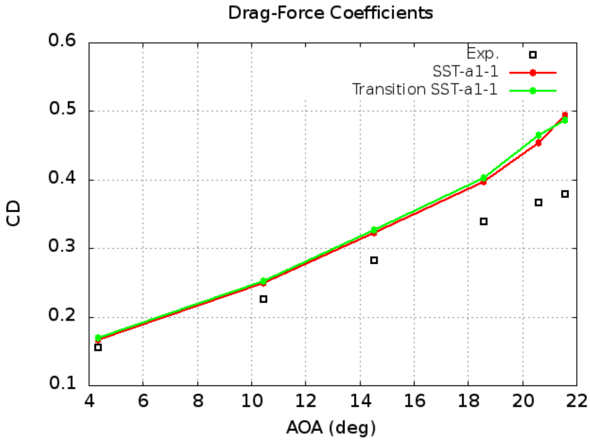

(b) C_D vs α.

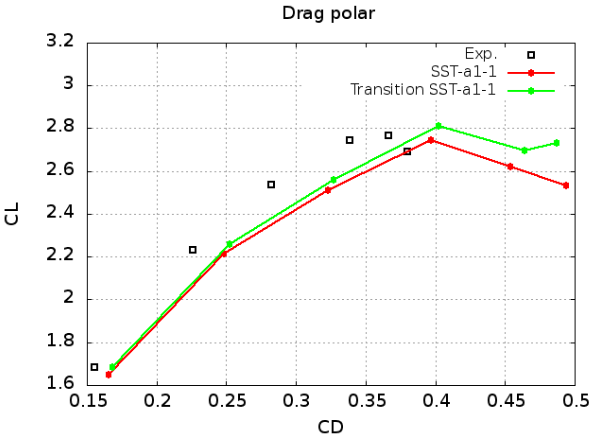

(c) C_L vs C_D.

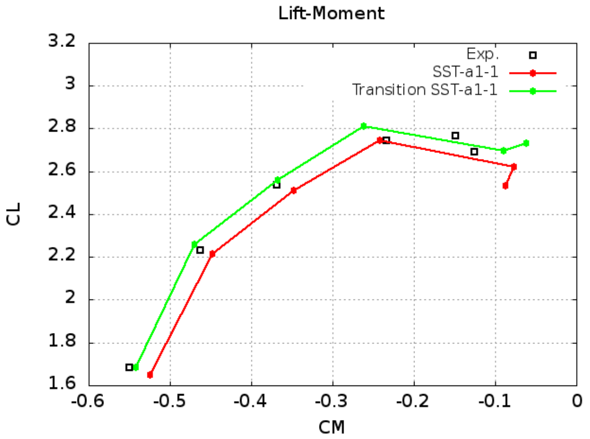

(d) C_L vs C_M.

Figure 4: JSM, Aerodynamic force coefficients for angles of attack sweep.

5.2 Experimental Oil Flow and C_p Comparisons

Comparisons between the surface flow patterns and C_p plots of the experimental and computational results for both models provide further insights. The spanwise C_p extraction locations are shown in Figure 5. At α=4.36^0, computational results (Figure 8), generally show good agreement with the experimental C_p data. The SST-Transition *a1=1* results generally show improved C_p comparison close to the suction peaks of all leading edges. The experimental data shows slightly larger suction peaks on the flap's leading edges when compared to the computational results, especially on stations inboard of the *Yehudi* break, with SST-Transition *a1=1* showing better agreement. The better agreement suggests that flow on the leading edge of the flap transitions from laminar to turbulent, as the china-clay visualization in (Figure 6) also indicates. The effect of the FTFs on the flaps are also visible on the china-clay visualization, with the leading edge experiencing turbulent flow, while a spiral vortex forms at its inboard trailing edge, as seen in the oil-flow visualization of Figure 7. Both these phenomena are well captured by the SST *a1=1* and SST-Transition *a1=1* computations, as seen in Figure 7. Both SST *a1=1* and SST-Transition *a1=1* show Side of Body (SOB) flow separation similar to the oil flow visualization, seen as a trailing edge vortex on the flap's upper surface.

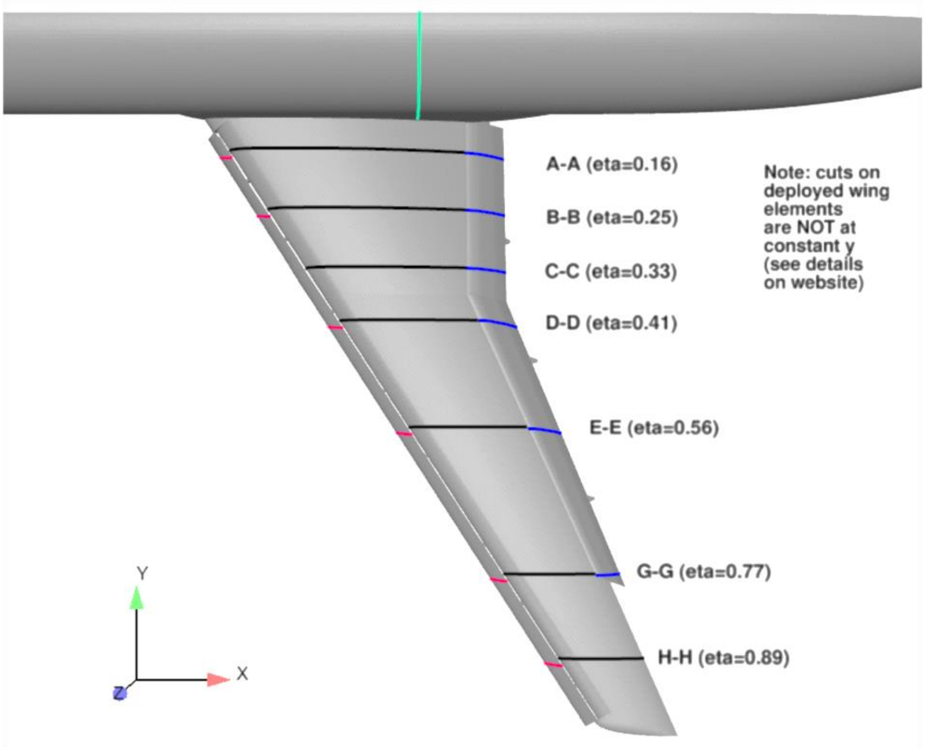

Figure 5. JSM Wing C_p Extraction Stations[4].

Additionally, the effect of slat support wakes can be seen on the wing surface in both computational and experimental results. The surface flow patterns in Figure 7 indicate that the flow behavior at the wing tip matches well with the oil flow visualization. The wing tip vortices are depicted well, forcing flow coming from upstream and the slat tip to move inward, before straightening out and eventually getting directed outward to the wing tip's trailing edge. In addition, the wing tip vortices together with the outermost outboard slat support wake result in the birth of a small wing trailing edge vortex. The transition behavior on the slat and flap seen on the china clay visualization (Figure 6) are matched well with SST-Transition *a1=1* model, though the SST-Transition *a1=1* model shows a large laminar section on the leading edge of the mid-wing section, which is absent in the experiment.

Figure 6. JSM with nacelle pylon - Visualization of boundary layer transition by china-clay at α=4.36^0 & comparison with SST-Transition *a1=1* computation results (JSM without nacelle pylon).

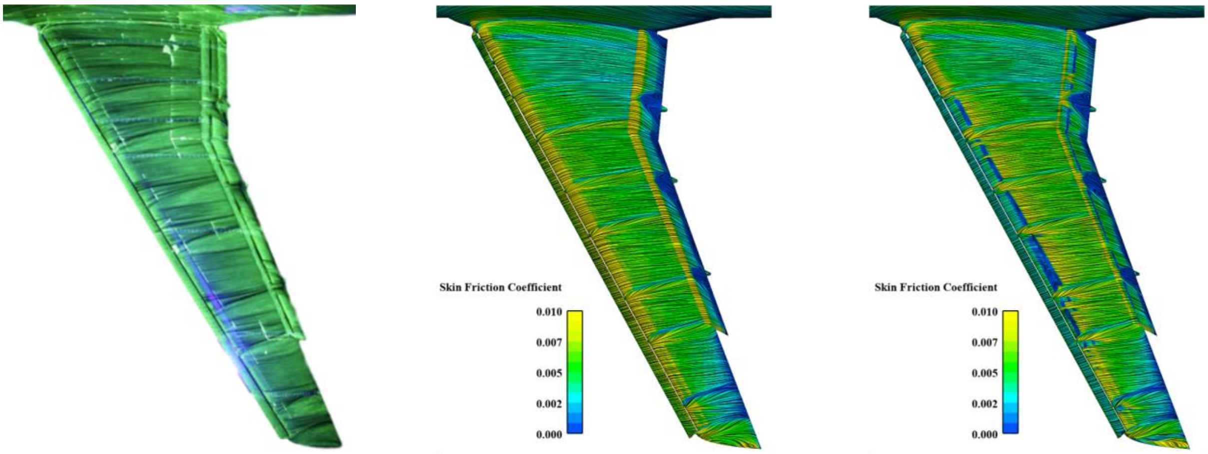

(a) Exp. Oil Flow.

(b) SST *a1=1*

(c) Transition SST *a1=1*.

Figure 7. JSM, Experimental Oil Flow vs. CFD Surface Flow Pattern at α = 4.36^0.

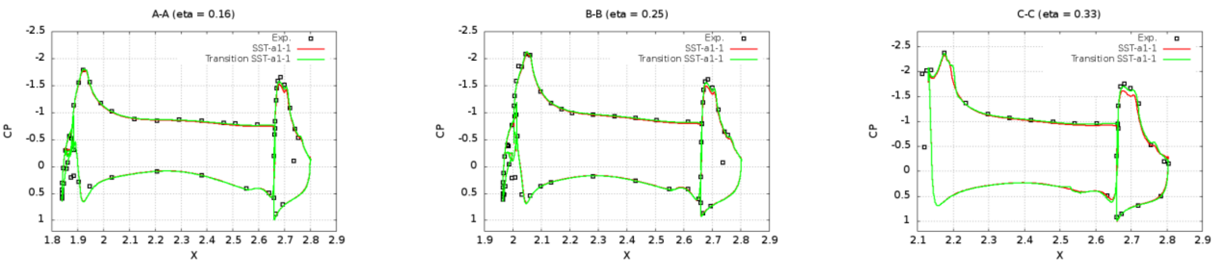

(a) A-A (eta=0.16).

(b) B-B (eta=0.25).

(c) C-C (eta=0.33).

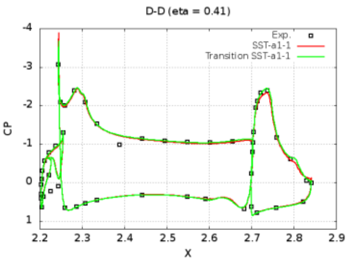

(d) D-D (eta=0.41).

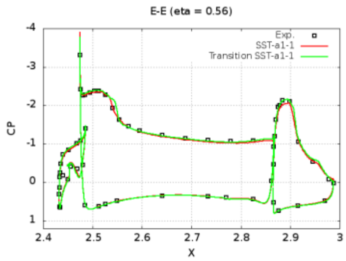

(e) E-E (eta=0.56).

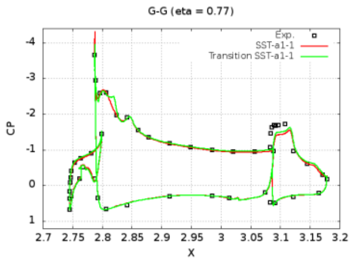

(f) G-G (eta=0.77).

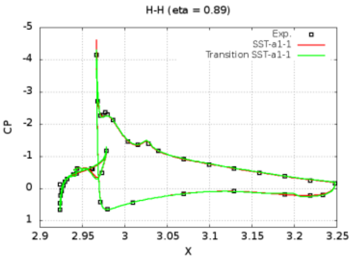

(g) H-H (eta=0.89).

Figure 8. JSM, C_p Plots Comparison with Experimental Measurements at $\alpha = 4.36^0$.

Figure 9. JSM with nacelle pylon - Visualization of boundary layer transition by china-clay at α=10.47^0 & comparison with SST-Transition *a1=1* computation results (JSM without nacelle pylon).

At α=10.47^0, both models show similar results to those at α=4.36^0, with generally larger suction peaks observed in the former (Figure 11). Additionally, both the experimental oil flow visualization and the computational surface flow patterns show larger wing tip vortex structures that locally influence the outboard wing flow patterns resulting in an additional small wing trailing edge spiral vortex structure forming beside the one seen at α=4.36^0. The transition behavior on the slat and flap seen on the china clay visualization (Figure 9) are matched well with SST-Transition *a1=1* model except at certain mid-slat locations where the onset of trailing edge turbulence is observed in the experiment but not in the computation. Also, the china clay visualizations show turbulent inboard wing leading edges, whereas the SST-Transition simulation indicates large regions of laminar flow – however the simulation does not include the nacelle, so this may be a cause for this difference.

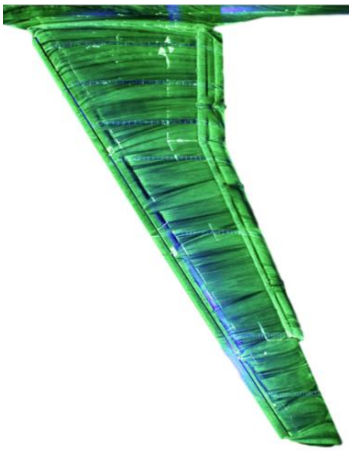

(a) Exp. Oil Flow.

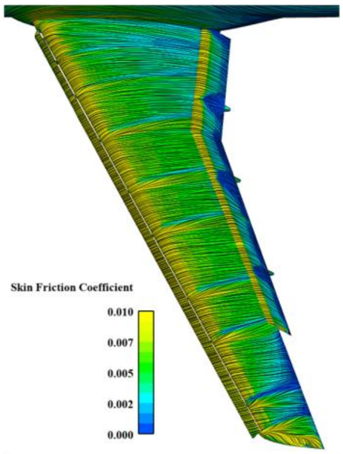

(b) SST *a1=1*.

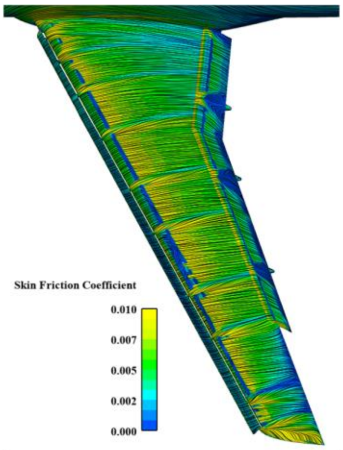

(c) Transition-SST *a1=1*.

Figure 10. JSM, Experimental Oil Flow vs. CFD Surface Flow Pattern at α = 10.47^0.

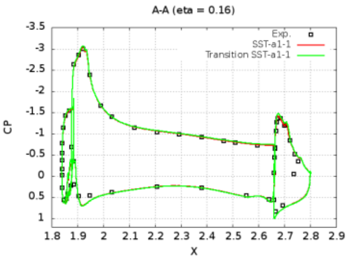

(a) A-A (eta=0.16).

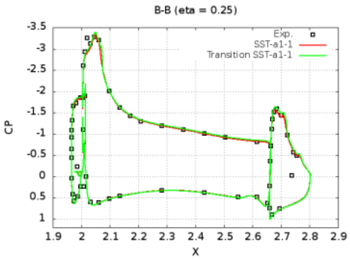

(b) B-B (eta=0.25).

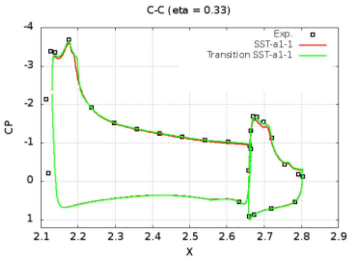

(c) C-C (eta=0.33).

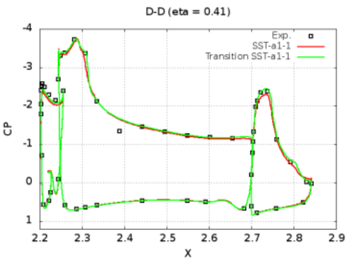

(d) D-D (eta=0.41).

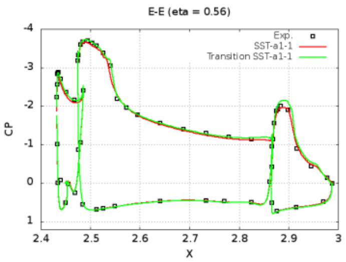

(e) E-E (eta=0.56).

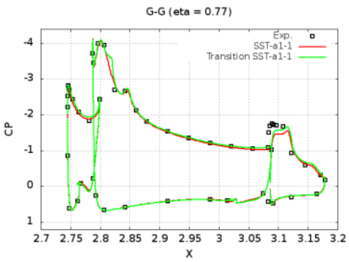

(f) G-G (eta=0.77).

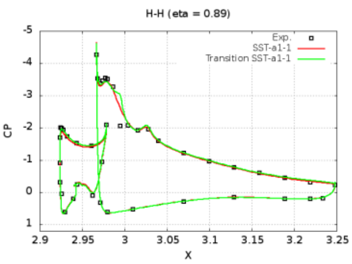

(g) H-H (eta=0.89).

Figure 11. JSM, C_p Plots Comparison with Experimental Measurements at α = 10.47^0.

At α=14.54^0, both models show good C_p agreement with experiment (Figure 13) for all stations except H-H, with the SST-Transition *a1=1* showing the better result. Computational surface flow patterns show flow deceleration near the outboard slat (resulting in smaller suction peaks) due to separation seen on most of the outboard wing upper surface. There are no experimental pictures available at this α but based on the α=18.58^0 experimental oil flow visualizations, this separation should not be observed.

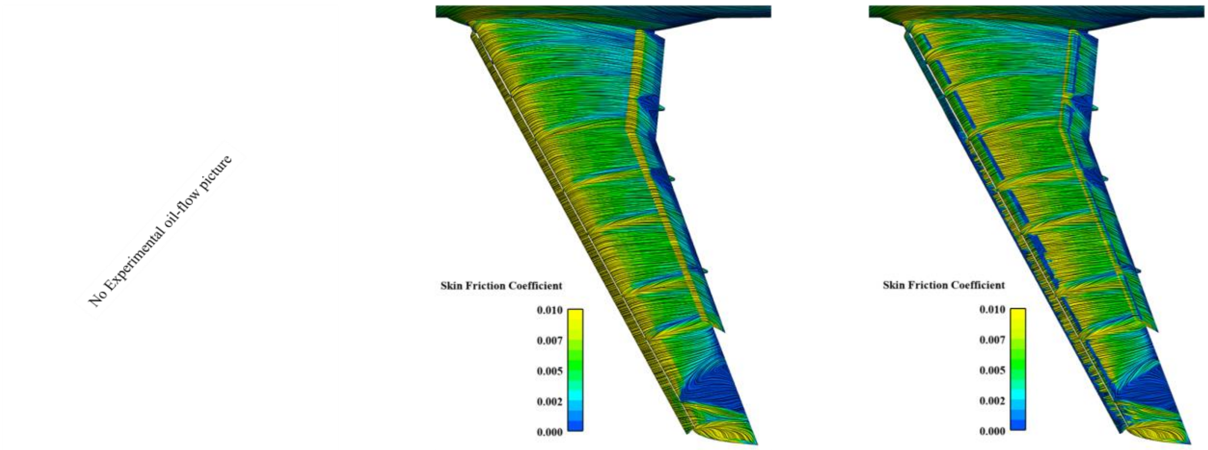

(b) SST *a1=1*

(c) Transition-SST *a1=1*

Figure 12. JSM, Experimental Oil Flow vs. CFD Surface Flow Pattern at α = 14.45^0.

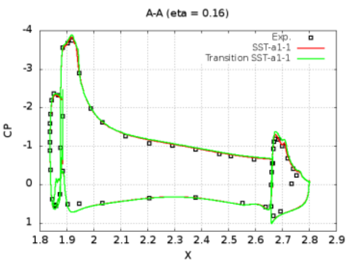

(a) A-A (eta=0.16).

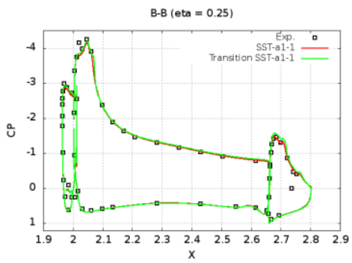

(b) B-B (eta=0.25).

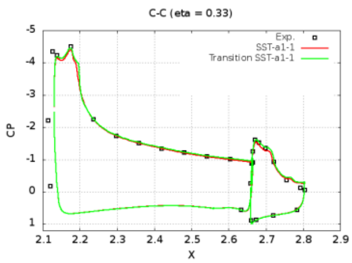

(c) C-C (eta=0.33).

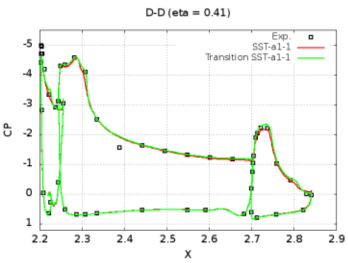

(d) D-D (eta=0.41).

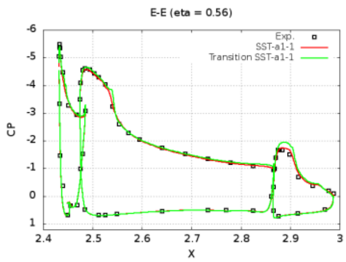

(e) E-E (eta=0.56).

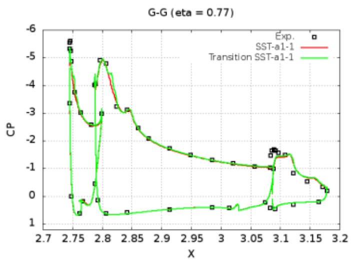

(f) G-G (eta=0.77).

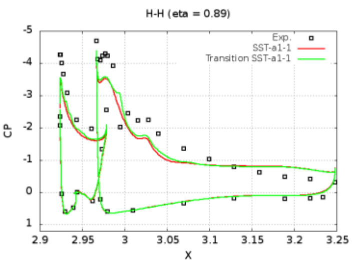

(g) H-H (eta=0.89).

Figure 13. JSM, C_p Plots Comparison with Experimental Measurements at α = 14.45^0.

In both SST *a1=1* and SST-Transition *a1=1*, the smaller outboard wing trailing edge spiral vortex formed earlier at $\alpha=4.36^0$, appears to have expanded to occupy a majority of the upper outboard wing surface, and together with the turbulent wakes from the outer most slat support, led to the outboard wing leading edge separation. This would also explain the higher drag predictions noted previously in the C_D-α, and C_L-C_D plots. Insufficient mesh resolution seems the most likely cause for this large unexpected separation to occur. In general, the slat leading edges are now producing less suction peaks (stations D-D, E-E, G-G and H-H) as compared to experimental C_p plots, with the SST-Transition *a1=1* now depicting transition to turbulence due to laminar separation, a phenomenon not seen at lower angles of attack. These differences at $\alpha=14.54^0$ suggest that further mesh refinement may be required in multiple areas: at the leading and trailing edges of outboard multi-element devices, in and around the outermost slat support and its wake, on the slat and wing tip, and finally around the outboard slat cove. Additional investigations are required to confirm this premise and improve understanding of the highly complex flow interactions occurring at these locations.

The computed surface flow patterns for both models at $\alpha=18.58^0$ are quite similar to the results at $\alpha=14.54^0$, especially in the outboard section of the wing. Again, good agreement in the pressure distribution are generally observed for both SST *a1=1* and SST-Transition *a1=1*, except at station H-H. The experimental oil flow visualization flow structures at the outboard wing separation area differ from the computational results. A small spiral vortex seen initially as a trailing edge vortex at $\alpha=4.36^0$, has moved and grown in strength. This vortex appears to interact with both the outermost slat support turbulent wake and the outboard wing trailing edge separation (caused by the larger wing tip vortices with larger axial spread). Possible reasons for some of these differences are as discussed previously. At the wing root and close to the wing-body and flap-body junctions, computational results generally match well, as seen by both the oil flow visualizations and the C_p plots. Encouragingly, computational results at $\alpha=18.58^0$ show the experimentally observed onset of wing SOB separation and wash out of flap SOB separation (seen earlier at lower angles of attack) at their respective trailing edges.

Figure 14. JSM with nacelle pylon - Visualization of boundary layer transition by china-clay at $\alpha=18.58^0$ & comparison with SST-Transition *a1=1* computation results (JSM without nacelle pylon).

Furthermore, the china clay visualizations (Figure 14) show that the SST- Transition *a1=1* results agree well with the laminar and turbulent regions on the leading edges of the multi-element wing, except at the leading edge of the inboard wing where turbulent flow dominates, contrary to what is observed in the computational results – again with the presence of the nacelle in the experiments being a possible factor.

(a) Exp. Oil Flow.

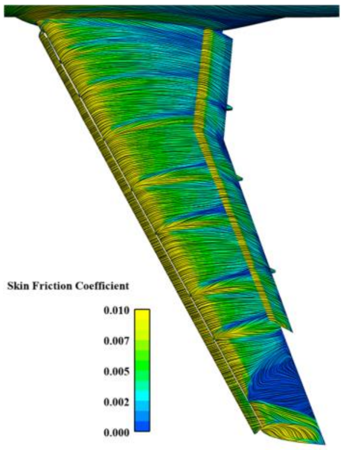

(b) SST *a1=1*.

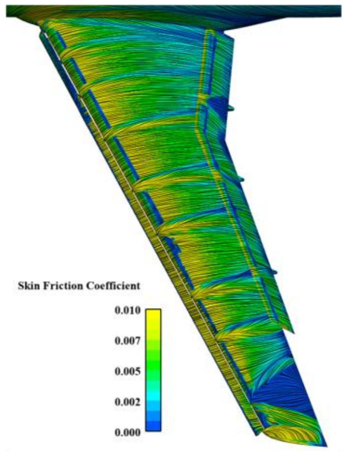

(c) Transition-SST *a1=1*

Figure 15. JSM, Experimental Oil Flow vs. CFD Surface Flow Pattern at $\alpha = 18.58^0$.

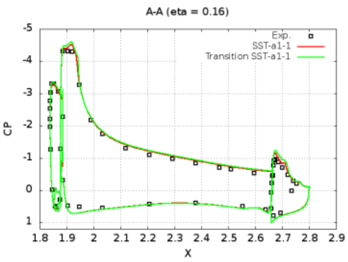

(a) A-A (eta=0.16).

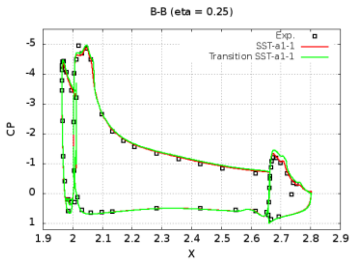

(b) B-B (eta=0.25).

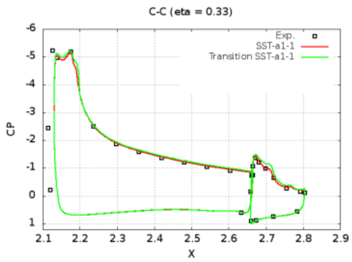

(c) C-C (eta=0.33).

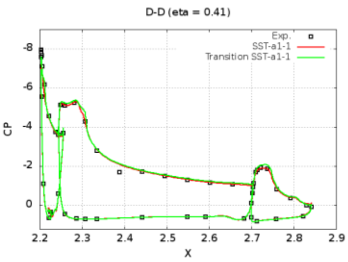

(d) D-D (eta=0.41).

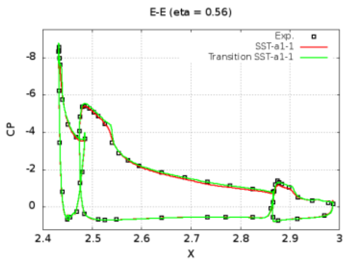

(e) E-E (eta=0.56).

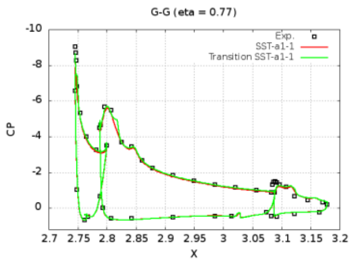

(f) G-G (eta=0.77).

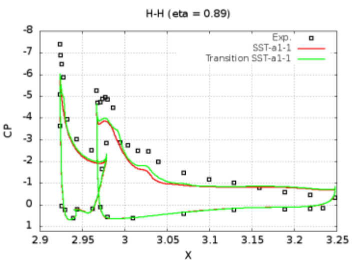

(g) H-H (eta=0.89).

Figure 16. JSM, C_p Plots Comparison with Experimental Measurements at $\alpha = 18.58^0$.

At α=20.59⁰, good agreement in the pressure distribution are generally observed for both SST *a1=1* and SST-Transition *a1=1*, except at station G-G and H-H. Both models capture a similar outboard wing leading edge separation in addition to a second large wing leading edge separation close to station G-G, the latter not likely to occur based on α=21.57⁰ experimental oil flow visualizations. This also explains the lower suction peaks at the slat leading edges (stations G-G and H-H) as compared to experimental C_p plots.

No Experimental oil-flow picture

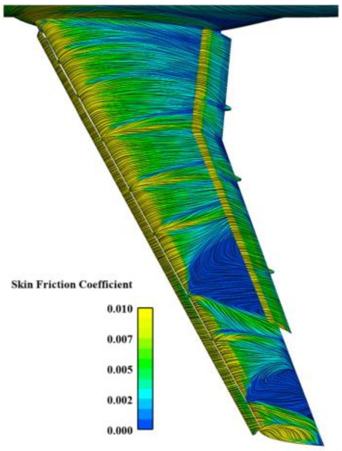

(b) SST *a1=1*.

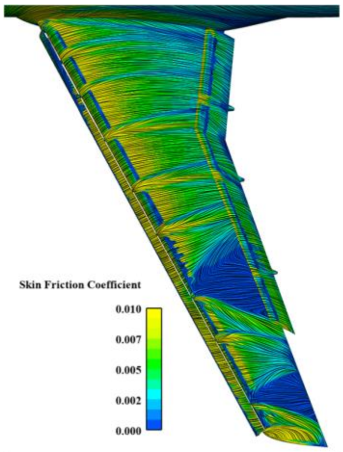

(c) Transition-SST *a1=1*.

Figure 17. JSM, Experimental Oil Flow vs. CFD Surface Flow Pattern at α = 20.59⁰.

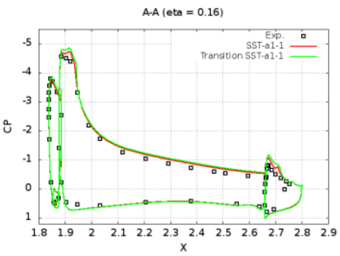

(a) A-A (eta=0.16).

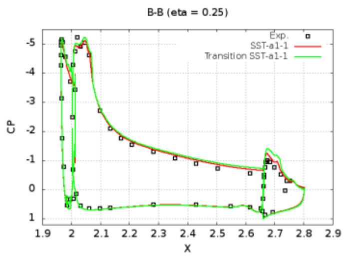

(b) B-B (eta=0.25).

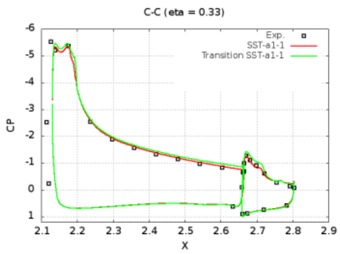

(c) C-C (eta=0.33).

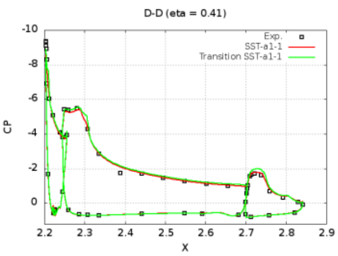

(d) D-D (eta=0.41).

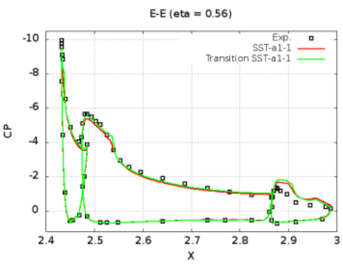

(e) E-E (eta=0.56).

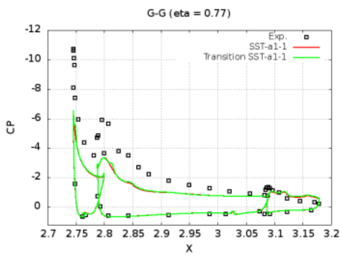

(f) G-G (eta=0.77).

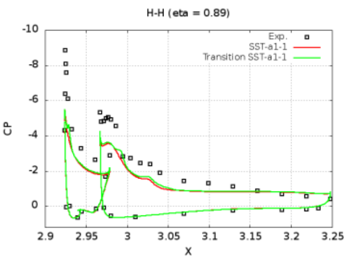

(g) H-H (eta=0.89).

Figure 18. JSM, C_p Plots Comparison with Experimental Measurements at α = 20.59⁰.

Differences noted earlier were primarily believed to be due to insufficient mesh resolution, and that also holds here. At the wing root and close to the wing-body and flap-body junctions, computational results generally match well, as seen by both the oil flow visualizations and the C_p plots. The computational results show increase in spread of the wing SOB separation. The close agreement between predicted surface pressure distributions at stations A-A and B-B and experimental data are consistent with this observation.

At α=21.57^0, the highest angle of attack simulated, experimental oil flow visualizations show that flow over the wing-body junction and a majority of the wing outboard section (outward of H-H station) are now separated, resulting in wing stall. The experiment exhibits a wing SOB separation that has a wide axial spread (starting at the mid-span root wing-body junction and ending further downstream at the wing's trailing edge location (upstream of the inboard FTF)) due to the large spanwise flow movement experienced. The flow separation behavior and vortex structures, locations and strengths differ between SST *a1=1* and SST-Transition *a1=1*. Some of these flow phenomena have been captured well by computation and, depending on the turbulence model, may be closer to experiment. For instance, the SST *a1=1* model does a better approximation of the spread of the wing SOB separation (Figure 19) than the SST-Transition *a1*=1 model, as also reflected in the C_p plot comparisons with experimental data of Figure 20 (stations A-A and B-B). However, it does not capture the same spanwise spread of the wing SOB separation that the experiment shows. On the other hand, the SST-Transition *a1=1* shows better comparisons with experimental oil-flow visualizations and surface pressure distributions on the mid-wing's upper surface. While both models capture similar outboard wing leading edge separation, it does not capture the trailing edge flow separation or the spiral vortex past the slat support in a similar manner. In addition, both SST *a1=1* and SST-Transition *a1=1,* predict a second large wing leading edge separation close to station E-E and G-G respectively, both not seen in experiment. Previously stated conclusions as to the possible cause for failure to capture these complex flow phenomena, apply here. Central to these conclusions are the need for further mesh refinement in key areas in order to achieve grid-independent solutions.

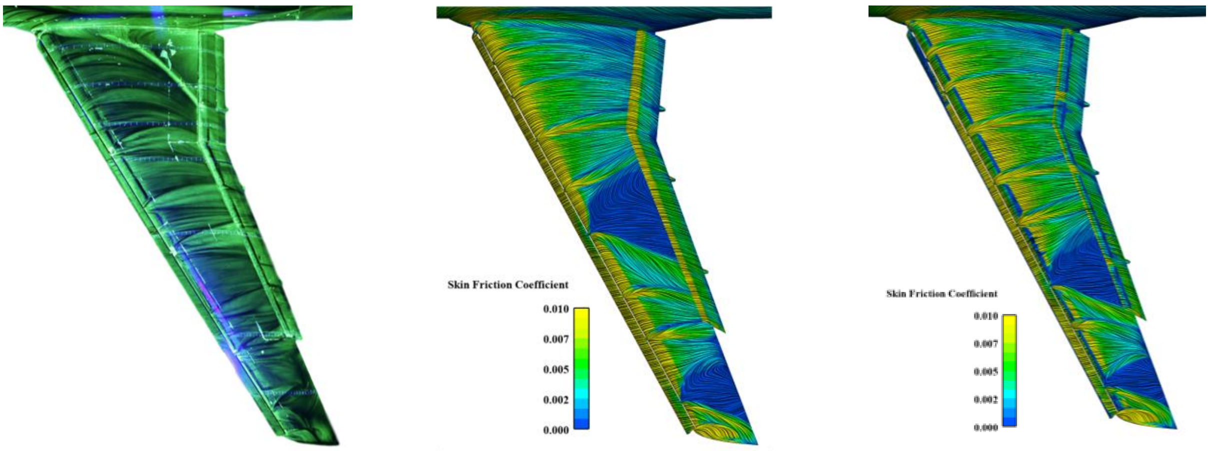

(a) Exp. Oil Flow. (b) SST *a1=1*. (c) Transition-SST *a1=1*.

Figure 19. JSM, Experimental Oil Flow vs. CFD Surface Flow Pattern at α = 21.57^0.

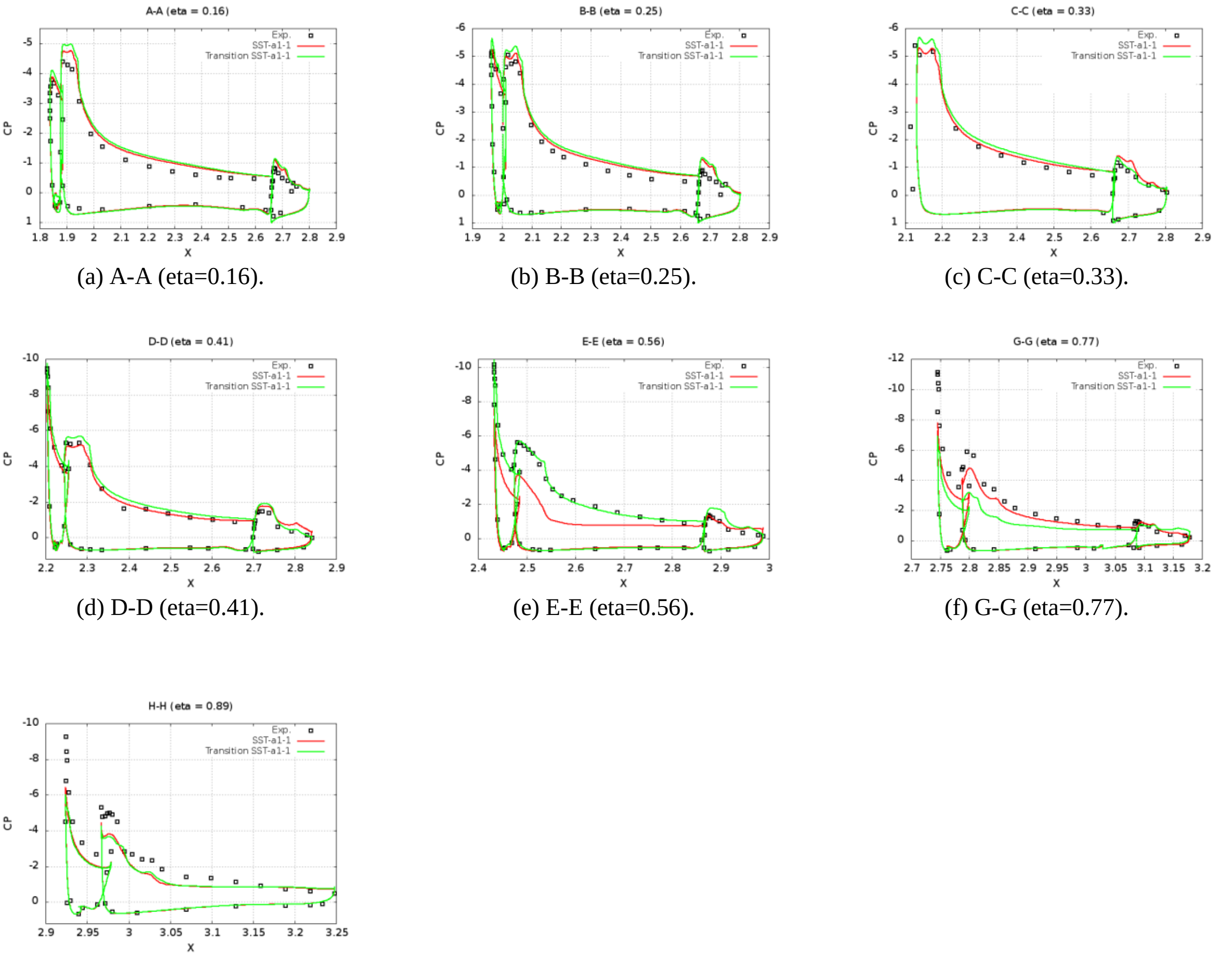

(a) A-A (eta=0.16).

(b) B-B (eta=0.25).

(c) C-C (eta=0.33).

(d) D-D (eta=0.41).

(e) E-E (eta=0.56).

(f) G-G (eta=0.77).

(g) H-H (eta=0.89).

Figure 20. JSM, C_p Plots Comparison with Experimental Measurements at $\alpha = 21.57^0$.

5.3 Mesh Considerations

Accurately predicting complex flow physics is highly dependent on mesh resolution and this is examined by comparing the solutions on two different meshes at $\alpha = 4.36^0$ with SST $a1=1$ turbulence model. One solution was obtained using ANSA-supplied mesh[21] (results presented at AIAA AVIATION 2018) and the other from using Fluent Meshing (details presented in this paper). Viscous wake interaction is one of the most important phenomena for the high-lift configurations. For example, adverse pressure gradient separation wakes on slat and wing upper surfaces interact with SOB separation wakes from the support brackets passing through gaps between slat-wing and wing-flaps over the upper surfaces of wing and flaps. In general, poor resolution of the wakes leads to their spread being overpredicted, and ultimately lowering the lift and increasing drag. This is consistent with the results seen in Figure 21 compared to Figure 22, and the higher drag predicted for the Fluent Mesh (the same observation can also be made further outboard, although this is not shown here).

The complex recirculation pattern seen in the cove behind the slat is also evident in these images, and the different meshes clearly have an impact on the predictions here, too, which in turn can strongly affect the flow impinging on the leading edge of the main wing and then entering the gap between slat and main wing. The higher resolution of the slat cove regions in Fluent mesh compared to the ANSA mesh is essential to capture the free shear layers and the slat core vortex in the slat cavity. The higher eddy viscosity in slat cove region is indicative of a better resolved slat cove vortex with the Fluent mesh compared to the ANSA mesh.

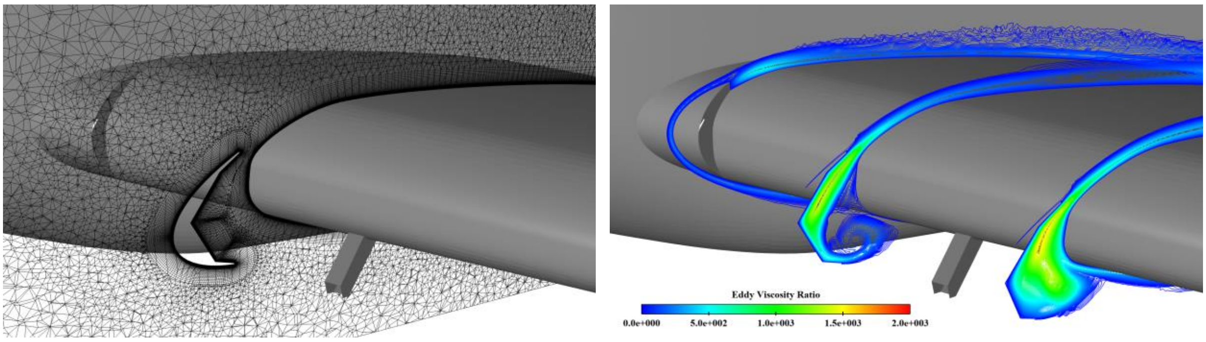

Figure 21. JSM ANSA-Mesh, Eddy Viscosity Ratio contours near wing root slat cove at $\alpha = 4.36^0$.

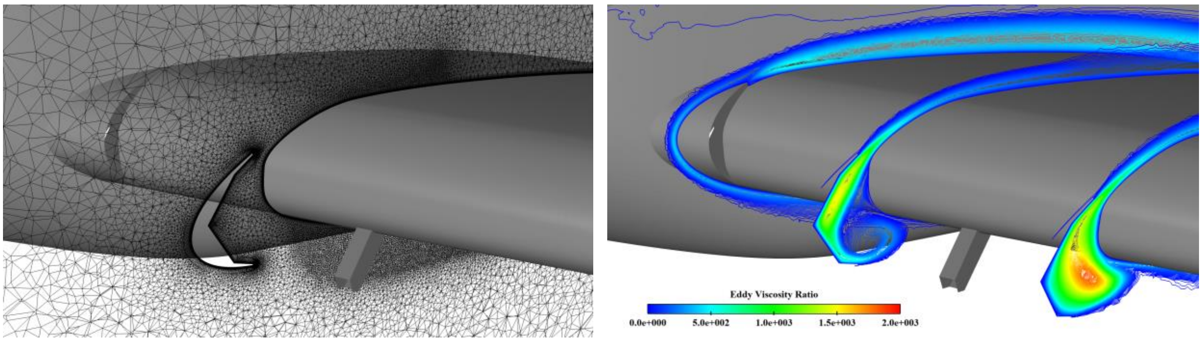

Figure 22. JSM Fluent-Mesh, Eddy Viscosity Ratio contours near wing root slat cove at $\alpha = 4.36^0$.

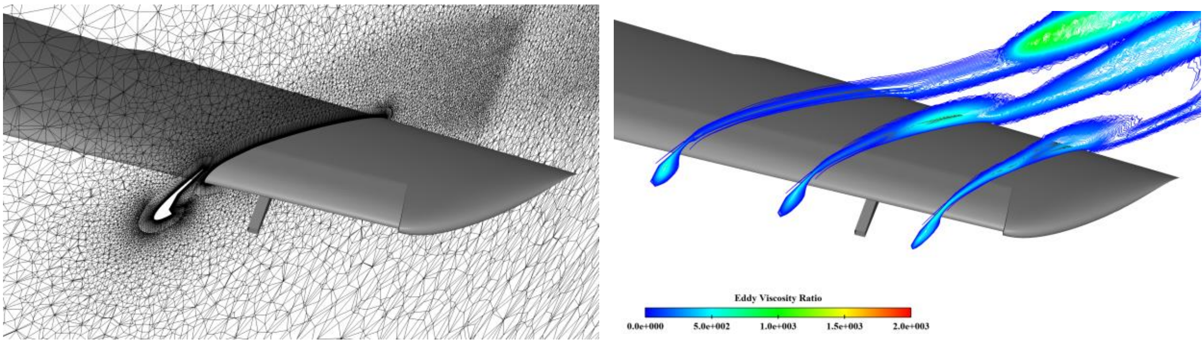

Figure 23. JSM ANSA-Mesh, Eddy Viscosity Ratio contours near wing tip slat cove at $\alpha = 4.36^0$.

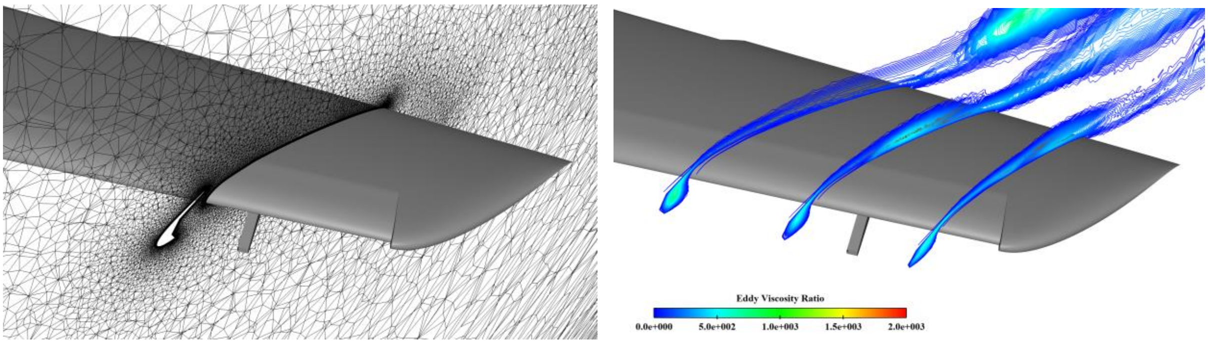

Figure 24. JSM Fluent-Mesh, Eddy Viscosity Ratio contours near wing tip slat cove at $\alpha = 4.36^0$.

Similarly, Figures 23 & 24 show eddy viscosity contours and mesh resolution at sectional cut planes near wing tip. Again, the slat cove vortex is slightly better resolved by the Fluent mesh, as indicated by slightly higher predicted eddy viscosity ratio compared to using ANSA mesh. Conversely, the flow around the wing and in the wing wake regions are better resolved by the ANSA mesh, as indicated by higher values and less spreading of eddy viscosity contours compared to the Fluent mesh.

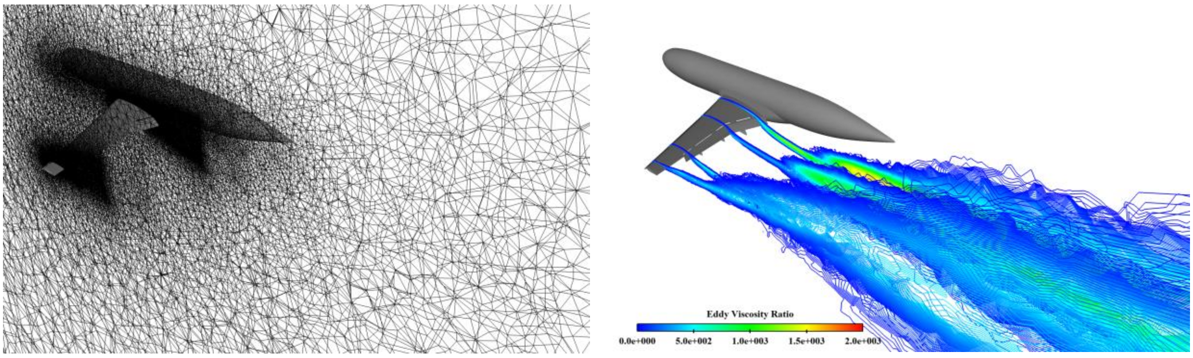

Figure 25. JSM ANSA-Mesh, Eddy Viscosity Ratio contours, wing span, zoom-out $\alpha = 4.36^0$.

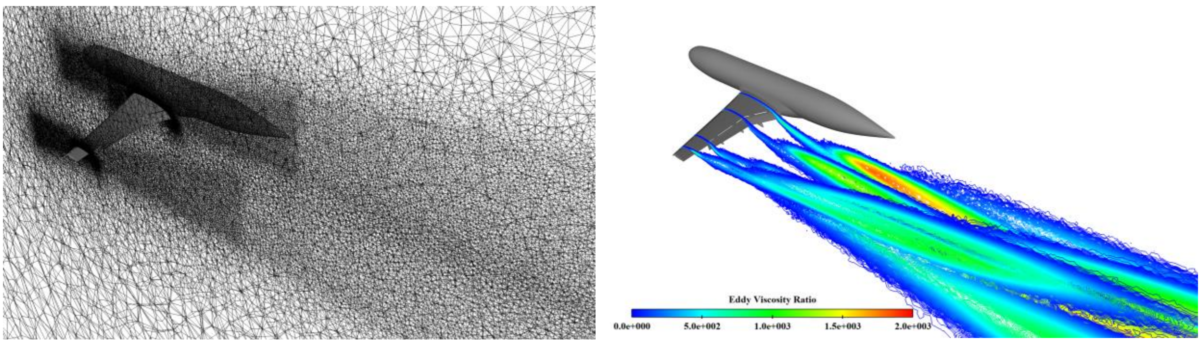

Figure 26. JSM Fluent-Mesh, Eddy Viscosity Ratio contours, wing span, zoom-out $\alpha = 4.36^0$.

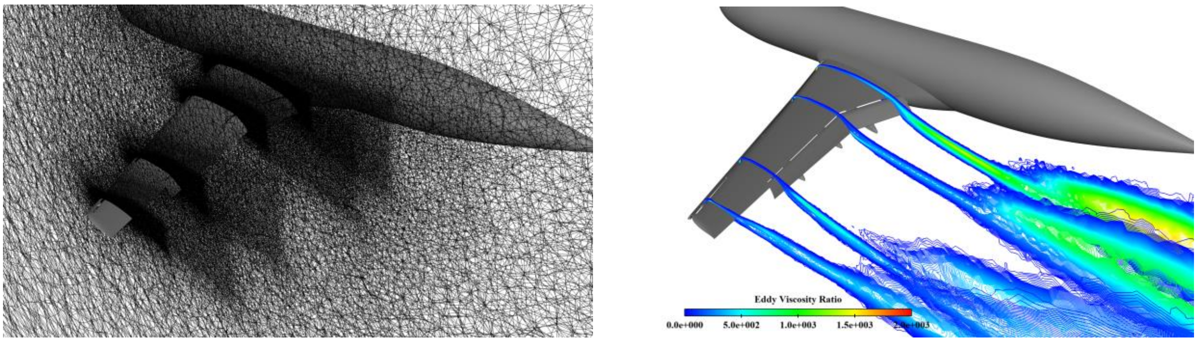

Figure 27. JSM ANSA-Mesh, Eddy Viscosity Ratio contours, wing span, zoom-in $\alpha = 4.36^0$.

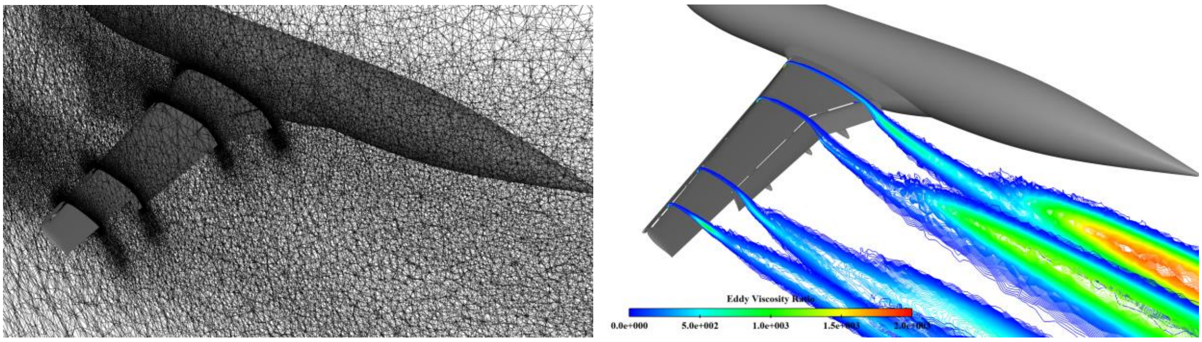

Figure 28. JSM Fluent-Mesh, Eddy Viscosity Ratio contours, wing span, zoom-in $\alpha = 4.36^0$.

Figure 25 to 28 show several views of the wing wake mesh refinements and eddy viscosity contours at different sections. Sufficient wake refinement is very important for predictions of lift and drag. Both ANSA and Fluent meshes have been refined in the wing wake, but each is still found wanting in different regards. The ANSA mesh has good wake resolution over the wing and few chord lengths behind the flap trailing edge, but then coarsens quite abruptly. The Fluent mesh, on the other hand, could be more refined over the wing and immediately downstream, but then has better resolution further downstream.

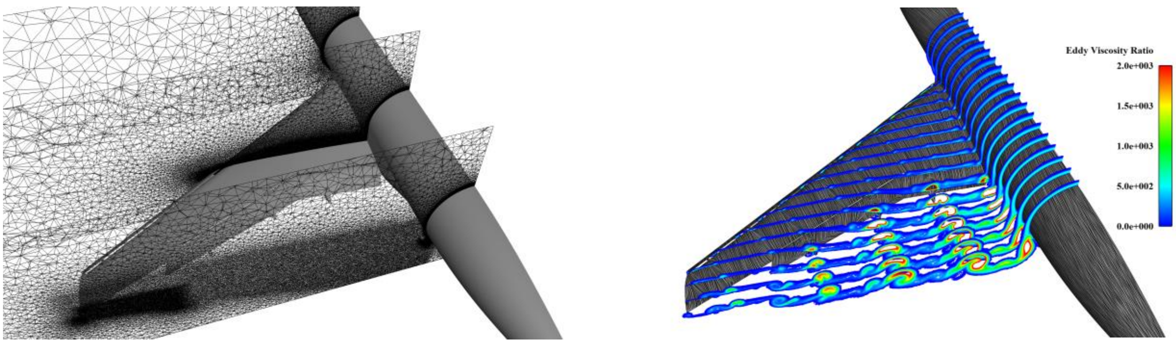

Figure 29. JSM ANSA-Mesh, Eddy Viscosity Ratio contours capturing wing wake $\alpha = 4.36^0$.

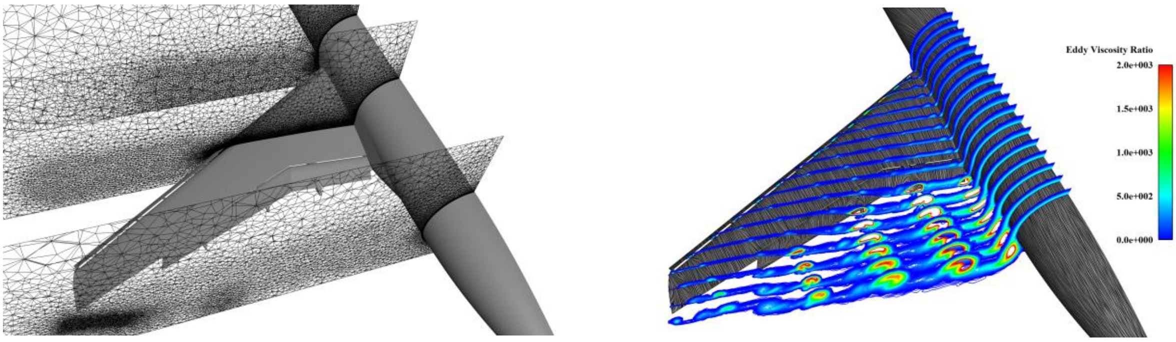

Figure 30. JSM Fluent-Mesh, Eddy Viscosity Ratio contours capturing wing wake $\alpha = 4.36^0$.

Figures 29 & 30 show the overall wing span wake originating from slat-tracks and passing over wing and flap using both the ANSA and Fluent meshes and highlight the development and propagation of wakes on multiple sectional cuts along the chord. Here again, the higher resolution of the ANSA mesh in the more immediate vicinity of the wing leads to better capturing of the wakes compared to solutions using the Fluent mesh.

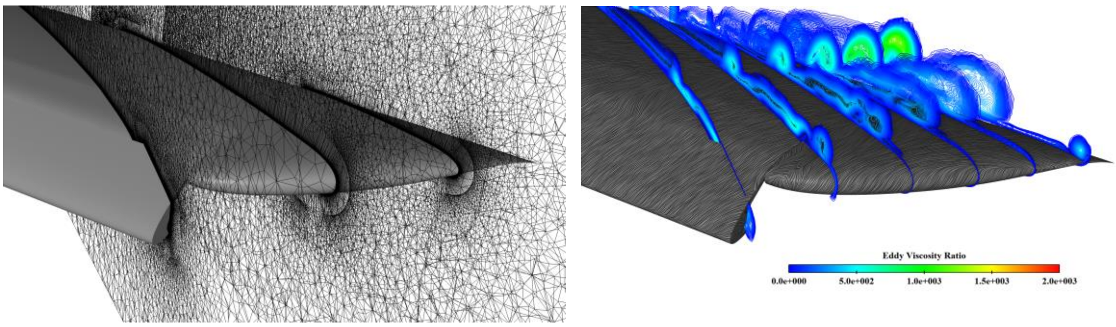

Figure 31. JSM ANSA-Mesh, Eddy Viscosity Ratio contours capturing wing-tip wake $\alpha = 4.36^0$.

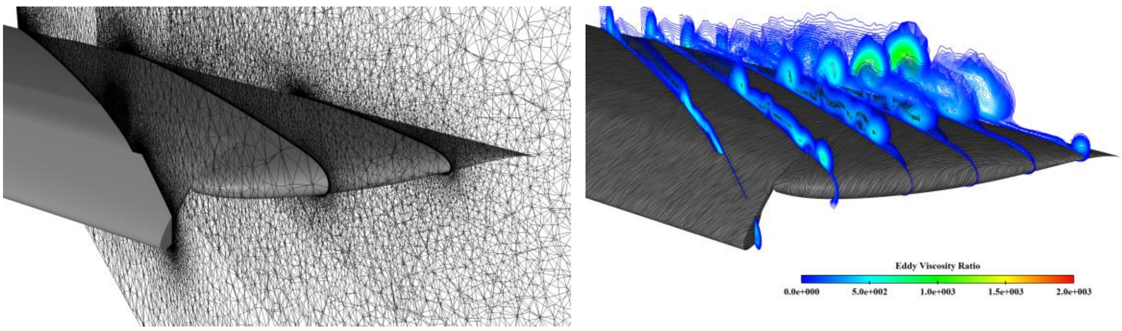

Figure 32. JSM Fluent-Mesh, Eddy Viscosity Ratio contours capturing wing-tip wake $\alpha = 4.36^0$.

Figure 31 & 32 shows the flow development around the wing-tip, with vortices originating from the slat track and the gap between slat and wing. The ANSA mesh with more mesh refinement in this area captures these more accurately compared to the Fluent mesh, as the eddy viscosity contours show.

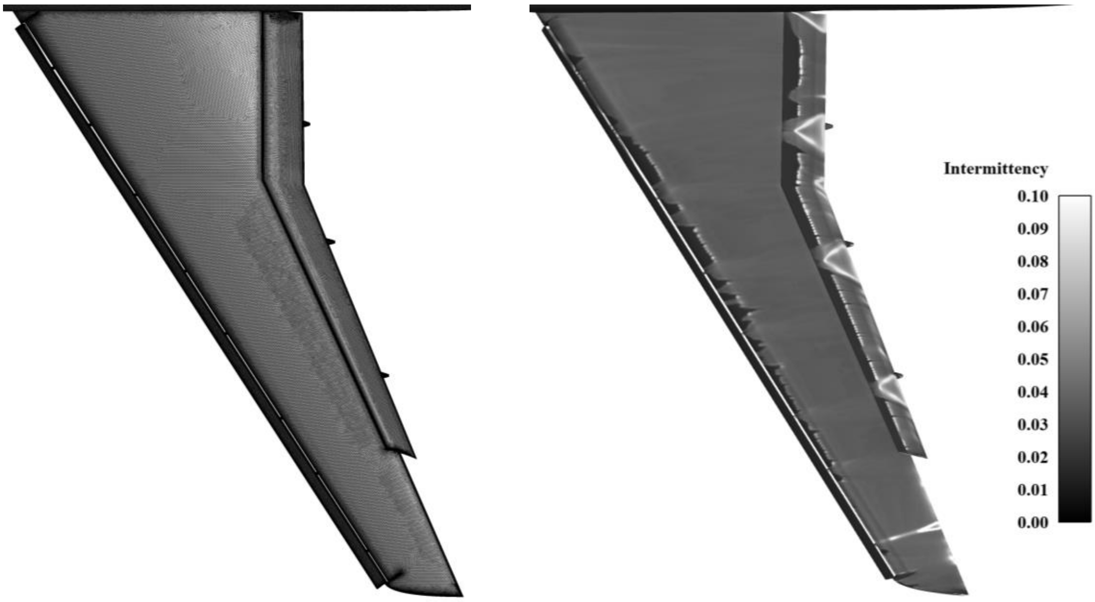

Figure 33. JSM ANSA-Mesh, surface mesh (left) and intermittency contours (right) at α = 4.36^0.

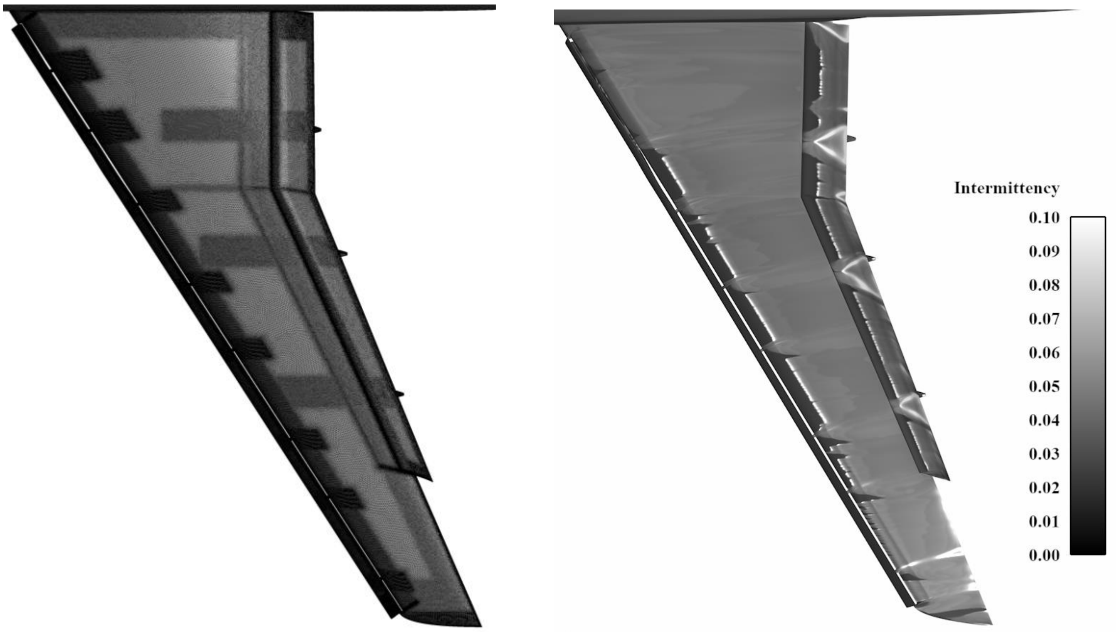

Figure 34. JSM Fluent-Mesh, surface mesh (left) and intermittency contours (right) at α = 4.36^0.

The SST-Transition *a1=1* intermittency contours predicted with the two meshes at α = 4.36^0 are shown in Figures 33 & 34. The laminar-turbulence transition appears to be better resolved using the Fluent mesh than with the ANSA mesh, owing to the greater mesh refinement in this region. This is especially noticeable near the leading edge at the mid-span wing location.

Overall, these comparisons of the flow solutions obtained at α = 4.36^0 with the SST *a1=1* and the SST-Transition *a1=1* turbulence model on the two different meshes give a number of insights into the mesh requirements for capturing the complex flow physics of high lift configurations accurately, some of which would represent a combination of the resolution used in the two meshes.

6 Conclusion and Further Work

The JSM model was simulated with an ANSYS Fluent Meshing mesh using SST-Transition with *a1=1* and SST with *a1=1* at six angles of attack (α). Both the computational results with SST *a1=1* and SST-Transition *a1=1* show good agreement with the experimental data, but both predict a lower stall angle when compared to experiment. Large differences between wind tunnel and computational results were observed for drag in both models, especially with increasing angles of attack. These differences are believed to be primarily due to insufficient grid resolution and overly rapid decay of turbulent flow structures in key flow regions, such as high-lift device trailing edge wakes, support bracket wakes, wing-body junction flow, slat and flap cove vortices, flap and wing tip vortices and any other secondary spiral vortices. The inherent limitation of linear eddy-viscosity turbulence models which neglect the non-linear effects of turbulent, secondary and swirling flows may also be a contributing factor. The experimental oil flow and china clay visualizations provided a more detailed picture of the complex flow patterns around the high-lift system, and highlighted differences between the computations and experiments. Predictions of attachment line transition, wing-body junction flow, wing-tip flow and outboard wing separation were seen to differ notably times from some experimental results. However, computational surface flow patterns on the high-lift system that included the slat tracks and FTFs, showed qualitatively good agreement with experimental oil flow visualizations. Correctly predicting viscous wake interactions (especially past the slat tracks) and wing-tip vortices were key to the overall lift and drag calculations. A clear and significant difference to experimental results was the computational prediction of a large area of separation on the outboard wing that already occurred in both cases at $\alpha = 14.54^0$, a significantly lower angle of attack than seen in experiments. The causes for this early prediction of separation needs to be studied more thoroughly.

In general, further investigation has been identified as necessary for various aspects of modelling the complex flow physics around such multi-element high lift configurations. For one, results show that laminar-turbulent transition has a significant and important effect, as also seen in the china clay visualizations from the experiments, and therefore needs to be correctly accounted for. Also, the required mesh resolution for grid converged results still needs to be established, taking into consideration all key areas, which include not only boundary layers and geometric features, but also flow-interior regions likes wakes, wing tip vortices, cavities, and gaps.

7 Acknowledgement

The authors would like to thank the HiLiftPW3 organizing team for providing rich data for CFD solver comparisons. Also, the authors would like to thank David Whitaker from CRAY for his support, and generously recognize CRAY HPC for providing computational resources for performing these simulations. Many thanks to Florian Menter and Boris Makarov both from ANSYS, for reviewing the results and providing valuable inputs. Special thanks to Vinod Mahale and Gandhar Parkhi from ANSYS for assistance during volume mesh generation in ANSYS Fluent Meshing. Finally, thanks to Aditya Mukane and Udo Tremel, also from ANSYS, for providing timely help in geometry preparation in ANSYS SpaceClaim Direct Modeler.

Fluent Scalability on CRAY XC Series Supercomputers

The Cray XC system offers excellent parallel performance for ANSYS Fluent, with continued scaling to more than 2,000 cores for ~165-million-cell simulation, as seen in Figure . Cray and ANSYS are committed to delivering high performance computing capabilities that quickly bring aerospace applications to new heights of simulation fidelity. This project is just one example of how ANSYS and Cray collaborate to build robust solutions for a broad set of engineering simulations.

Cray XC40 system combines the advantages of its Aries™ interconnect and Dragonfly network topology, Intel® Xeon® processors, integrated storage solutions, and major enhancements to the Cray Linux® Environment and programming environment. The Cray XC40 supercomputer is a groundbreaking architecture upgradable to 100 petaflops per system.

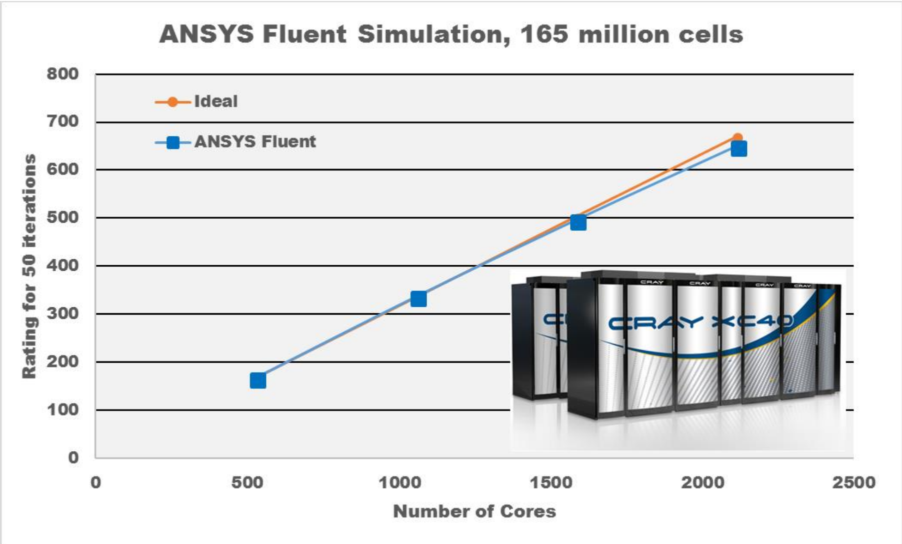

Figure 35 Performance chart of ANSYS Fluent Simulation on CRAY XC40 Supercomputers.

References

[1] Meredith, P. T., "*Viscous Phenomena Affecting High-Lift Systems and Suggestions for Future CFD Development*," High-Lift Systems Aerodynamics, AGARD CP-515, Sept. 1993, pp. 19-1–19-8.

[2] Mitsuhiro Murayama, Kazuomi Yamamoto, and Kunihiko Kobayashi. "*Validation of Computations Around High-Lift Configurations by Structured- and Unstructured-Mesh*", Journal of Aircraft, Vol. 43, No. 2 (2006), pp. 395-406.

[3] Murayama, Mitsuhiro Murayama, Yuzuru Yokokawa, Kazuomi Yamamoto, and Yoshine Ueda. "*CFD Validation Study for a High-Lift Configuration of a Civil Aircraft Model*", 25th AIAA Applied Aerodynamics Conference, 25 - 28 June 2007, Miami, FL

[4] *3rd AIAA CFD High Lift Prediction Workshop*, URL: http://hiliftpw.larc.nasa.gov/, email: hiliftpw@gmail.com, June 2015

[5] Menter, F. R., "*Two-Equation Eddy-Viscosity Turbulence Models for Engineering Applications*,"

AIAA Journal, Vol. 32, No. 8, pp. 1598-1605, (1994).

[6] Menter, F. R., Kuntz, M., and Langtry, R., "*Ten Years of Industrial Experience with the SST Turbulence Model,*" Turbulence, Heat and Mass Transfer 4, ed: K. Hanjalic, Y. Nagano, and M. Tummers, Begell House, Inc., 2003, pp. 625 - 632.

[7] Langtry, R. B. and Menter, F. R., "*Correlation-Based Transition Modeling for Unstructured Parallelized Computational Fluid Dynamics Codes*," AIAA Journal, Vol. 47, No. 12, December 2009, pp. 2894-2906.

[8] Hiroshi Kato, Keiichi Ishiko, and Akira Yoshizawa. "*Optimization of Parameter Values in the Turbulence Model Aided by Data Assimilation*", AIAA Journal, Vol. 54, No. 5 (2016), pp. 1512-1523.

[9] Ito, T., Ura, H., Yokokawa, Y., Kato, H., Mitsuo, K., and Yamamoto, K., "*High-Lift Device Testing in JAXA 6.5m×5.5m Low-speed Wind Tunnel*," AIAA Paper 2006-3643, June 2006.

[10] 5Ito, T., Ura, H., Yokokawa, Y., Kato, H., Mitsuo, K., and Yamamoto, K., "*Experimental and CFD of a High-Lift Configuration Civil Transport Aircraft Model*," AIAA Paper 2006-3452, June 2006.

[11] C. P. van Dam, "*The aerodynamic design of multi-element high-lift systems for Transport Airplanes*," Progress in Aerospace Science, Vol.38 101-144, 2002.

[12] Rumsey, C., Slotnick, J., Long, M., Stuever, R., Wayman, T., "*Summary of the First AIAA CFD High-Lift Prediction Workshop*," Journal of Aircraft, Vol. 48, No. 6, pp. 2068-2079, November-December 2011.

[13] Christopher L. Rumsey and Jeffrey P. Slotnick. "*Overview and Summary of the Second AIAA High-Lift Prediction Workshop*", Journal of Aircraft, Vol. 52, No. 4 (2015), pp. 1006-1025.

[14] Chaffin, M. S. and Pirzaheh, S., "*Unstructured Navier-Stokes High-Lift Computations on a Trapezoidal Wing*," AIAA Paper 2005-5084, June 2005.

[15] Yokokawa, Y., Murayama, M., Ito, T., and Yamamoto, K., "*Experimental and CFD of a High-Lift Configuration Civil Transport Aircraft Model*," AIAA Paper 2006-3452, June 2006.

[16] Smirnov, P., and Menter, F. R., "*Sensitization of the SST turbulence model to rotation and curvature by applying the Spalart–Shur correction term*," Journal of Turbomachinery, Vol 131, Issue 4, July 2009.

[17] Lei, Z., "*Effect of RANS Turbulence Models on Computational of Separated Flows over a Wing-Body Configuration*," Transactions of the Japan Society for Aeronautical and Space Sciences, Vol. 48, Nov. 2005, pp. 150-160.

[18] Rogers, S. E., Roth, K., and Nash, S. M., "*CFD Validation of High-Lift Flows with Significant Wind-Tunnel Effects*," AIAA Paper 2000-4218, Aug. 2000.

[19] Krumbein, A., "*Automatic Transition Prediction and Application to 3D High-Lift Configurations*," AIAA Paper 2006-3164, June 2006.

[20] Perraud, J. and Moens, F., "*Transport Aircraft 3D High Lift Wing Numerical Transition Prediction*," AIAA Paper 2007-264, Jan. 2007.

[21] Krishna, Z., Shoaib, S., John, S., Balasubramanyam, S., and Patrick, S., "*ANSYS CFD Study for High-Lift Aircraft Configurations*". Special Session: High Lift Prediction Using CFD, AIAA AVIATION, June 2018. Submitted.